Int J Adv Manuf Technol (2010) 47:731–743
DOI 10.1007/s00170-009-2211-8

ORIGINAL ARTICLE

A novel internal thread defect auto-inspection system

Der-Baau Perng · Ssu-Han Chen · Yuan-Shuo Chang

Received: 30 April 2009 / Accepted: 13 July 2009 / Published online: 30 July 2009

Abstract This paper describes a novel optical thread plug gauge (OTPG) for internal thread inspection using machine vision. The OTPG is composed of a rigid industrial endoscope, a charge-coupled device camera, and a two degree-of-freedom motion control unit. A sequence of partial wall images of an internal thread are retrieved and reconstructed into a 2D unwrapped image. Then, a digital image processing and classification procedure is used to normalize, segment, and determine the quality of the internal thread. The proposed OTPG provides an orientation-free and convenient method for detecting defects such as scratches, collapses, and flaws in an internal thread.

Keywords Internal thread · Rigid industrial endoscope · Machine vision · Directional texture · Fourier-based image restoration scheme

1 Introduction

An internal thread is a spiral screw pattern cut into the inner surface of a hollow cylinder. A thread pattern is composed of a crest, a root, and two flanks. The crest, the most prominent part of the thread pattern, is the plateau between the two slanted surfaces. The root is the bottom of the groove between the two slanted surfaces. The flanks are the slanted sides that connect the crest and root; these may be straight or curved.

D.-B. Perng (✉) · S.-H. Chen · Y.-S. Chang
Department of Industrial Engineering and Management,
National Chiao Tung University,
HsinChu 30010, Taiwan
e-mail: perng@cc.nctu.edu.tw

In the usual tapping process, a screw tap may leave material filings that form undesired shapes on the thread such as a collapse on the crest, a scratch on the flank, or a flaw in the root. A scratch on the flank is a significant bulge that can cause an internal thread to bind with an external one. A collapse on the crest or a flaw deep inside the root will decrease the ability of an internal thread to provide a tight fit. The internal threads in nuts have a wide variety of sizes, depths, and shapes. Due to the very nature of nuts and limited space, visually inspecting the internal thread is not a trivial task. The quality of an internal thread is difficult to guarantee since the entire thread pattern is difficult to see and some implicit defects may be overlooked.

A thread plug gauge is usually used to check the functionality of an internal thread by screwing the gauge into every thread manually. However, the screwing operation is labor-intensive, time-consuming, and subject to interference. Furthermore, a contact gauge cannot detect certain cave-shaped defects such as collapses or flaws. A noncontact inspection approach is required for the mass production of internally threaded components for the automobile, shipbuilding, and aerospace industries where high inspection rate is required.

Machine vision has rarely been used in the inspection of internal threads due to the unique structure and limited space available. We developed a novel internal thread inspection mechanism that relies on machine vision to create an optical thread plug gauge (OTPG) capable of overcoming the inherent dimensional limitations of internal threads. We used a rigid industrial endoscope, a charge-coupled device (CCD) camera, and a two degree-of-freedom motion control unit to capture a sequence of partial wall images of an internal thread without any mechanical contact. We used a 2D image registration method to reconstruct the unwrapped images and a digital image processing and classification procedure to determine the quality of the internal

threads. Forty-four internal thread images were used to validate the proposed OTPG. The successful detection rate was up to 97.72%, and it demonstrated that the OTPG detects the defects accurately and robustly.

The rest of this paper is organized as follows: In Section 2, we review related research. In Section 3, we describe the hardware structure and the software algorithm of the proposed automated optical inspection system. In Section 4, we describe the experimental environment and present the results. Our concluding remarks and further suggestions are discussed in Section 5.

2 Literature review

2.1 Noncontact internal thread inspection

Some promising new techniques for noncontact internal thread inspection have been developed in recent years. Four types of test are briefly described below.

1. Reflected light test [1–7]: The mechanism is equipped with a transmitter/receiver probe arranged perpendicular to the thread surface. The transmitter sends a light beam toward the thread, and the reflection goes back to the receiver. The reflectivity is used as a quantifiable feature for defect determination. Field summarized two drawbacks of the reflected light test [8]. First, when thread has been polluted by fluid or oil, varying levels of reflectivity can degrade the detection capability. Second, this technique senses only a small portion of the threaded hole due to the low scanning speed.
2. Magnetic flux leakage test [9, 10]: A magnetizer magnetizes a part of the internal thread to generate a magnetic leakage field. A detector detects the magnetic leakage field and transforms it into defect signals that can be used to identify defects in threads and mark their positions and ranges. The magnetic flux leakage test, however, can only be used on metal parts.
3. Eddy current test [11]: A probe generating an eddy current is inserted into the part with the internal thread. A sensor measures the response signals, which give only a rough indication of the screw defects and positions. Nevertheless, the eddy current test is sensitive to the material's microstructure, hardness, chemistry, temperature, and geometry.
4. Industrial computed tomography (CT) test [12]: The tomography of a part is retrieved from multiple directions and the system uses image processing to detect inner faults and measure their geometrical size. As with the reflected light test, this system only scans a small portion of the thread. Moreover, the CT equipment is very expensive.

2.2 Use of rigid industrial endoscope

It is impossible for an ordinary detector to look inside small-diameter holes to evaluate internal conditions. Crampton developed the first rigid endoscope in 1921 to check for possible flaws inside the rotor of a steam turbine [13]. The distinct characteristics of the endoscope are that it can extend the range of vision and change the angle of view to see what could not otherwise be seen. Modern endoscopes are complex, vital noncontact inspection instruments that include an optical–mechatronic sensor and an autocontrol scheme. In the past two decades, endoscopes have been used in a wide range of industrial applications. Parenti et al. used them to analyze the combustion in a burner [14]. Tsushima et al. employed them to inspect the inner walls of steel tubes for corrosion [15]. Boudjahi et al. developed an integrated system for detecting microcracks in pipes [16]. Gu used a video endoscope in civil aviation maintenance [17]. Biegelbauer et al. proposed a surface reconstruction system for bore holes using an endoscope [18]. Bondarev and Ahn et al. described numerous endoscope applications in the petroleum and gas industry [19–21]. These papers form a background for using the rigid endoscope in internal thread inspection.

2.3 Surface registration from a sequence of 2D images

Image registration is essential to evaluating the global surface texture. Registration aligns two or more images from different sensors or viewpoints. Some studies have used a sequence of 2D images to reconstruct the surface of an object for specific applications such as

1. Reconstructing a large object surface: printed circuit board [22], cathode ray tube panel [23], organic light-emitting diode panel [24], or thin film transistor liquid crystal display panel [25]
2. Reconstructing a nonflat object surface: bore hole [18] or router [26]
3. Reconstructing an object surface with high resolution: integrated circuit chip [27]

Registration techniques have been developed for many different types of problems. In general, the alignment methods can be separated into two categories according to whether two or more aligned images overlap or not. Both categories require close coordination of the sensor and an associated motion unit. For the nonoverlapping method, the region of interest (ROI) must exist in two successive but nonoverlapping images [18, 24]. For the overlapping method, the ROI must exist in two successive images that overlap by a specified percentage. The users must predefine the overlapping region in the first image as a template and then apply the pattern matching algorithm to the neighboring

image [28, 29]. In the matching process, the predefined template will slide over the entire target image on a pixel-by-pixel or subpixel-by-subpixel basis so that the maximum matching score can be found and the corresponding alignment coordinate can be determined [22, 23, 27]. Although the registration image of the former method may be rougher than the latter one, it is highly computationally efficient and so was used in this paper. It is worth to highlight that the nonoverlapping method adopted in the proposed OTPG relies on extremely good coordination between motion control and the sensor. Besides, it also requires that the sensor and thread coordinate systems (particularly their rotational axes) coincide extremely well.

2.4 Surface inspection for directional textures

Directional textures arise mainly in machined surfaces and textile fabrics. These consist of repetitive and periodic line primitives on the texture surface. Detecting local anomalies embedded in a directional texture surface is one of the important research problems in machine vision and can be broadly applied to surface quality control. Numerous approaches to the problem have been proposed: statistical, structural, spatial domain filtering, spectral domain filtering, and model-based approaches [30, 31]. Among the spectral approaches, the Fourier transform [32, 33], the wavelet transform [34–36], and the Gabor filter [37, 38] have been widely used in texture defect detection. An image processing method based on Fourier-based restoration was used in this paper.

3 Research method

3.1 OTPG hardware

The hardware system for internal thread extraction is shown in Fig. 1. The sequences of internal thread images were captured by a TELI CS8320 black and white camera with a resolution of 640×480 and a Matrox Meteor II frame grabber. A CCD with an illumination less than 0.4 lux is recommended for this task. A 7-in. Hawkeye Slim rigid industrial endoscope connected to a 90° side-view mirror tube was used as the lens. The outside diameter of the endoscope was only 0.20 in. and included a compact illumination fiber. The Moritex MHF-G150LR halogen light source supplied white light to the endoscope to enable the CCD to receive clear images in dark cavities. To overcome the line of sight limitation of the 90° side-view adaptor, the mechanism included a rotational servo motor (SM3416D_PLS) and a linear actuator (SmartT integrated module) to observe all the surfaces of the internal thread at different successive angles and depths. The apparatus was

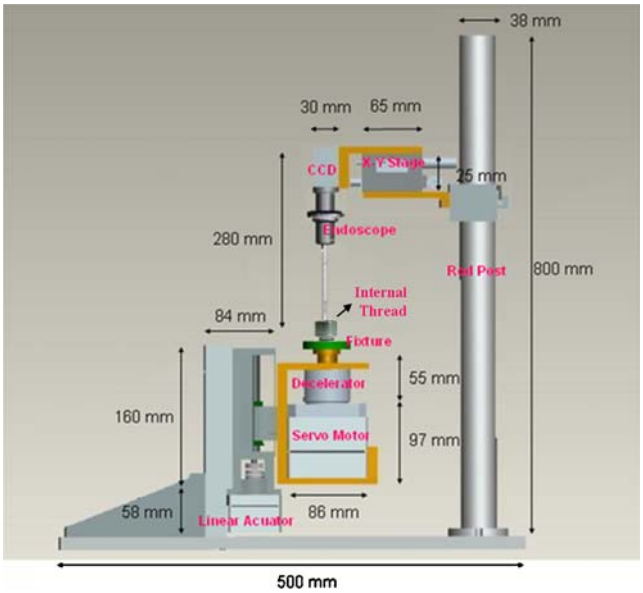

Fig. 1 Proposed OTPG hardware

connected to a computer. A flowchart of the proposed vision inspection method is given in Fig. 2. The details of this method are described below.

3.2 Registration of the 2D unwrapped image

The inner surface of internal thread can be fully observed by the proposed OTPG. Even so, image distortion and nonuniform illumination will occur due to the inherent endoscope structure and the cylindrical geometry of the internal threads. The farther away the pixels are from the center of the captured image, the more significant the above phenomena will be. Thus, we used only the region with little distortion near the center of each image for various angles and depths.

With appropriate control of the sensor and the associated motion unit, we could extract a sequence of 20×20-pixel low-distortion images by rotating the fixture in 2° steps. The field-of-view for each subimage is about 0.267×0.267 mm^2. The ROI of two successive images under these conditions is restricted to only two nonoverlapping neighbors. After the fixture has rotated 360°, the linear actuator raises the fixture to the next level and the rotation is repeated. The procedure continues until images of all the inner surfaces of the internal thread have been captured. Finally, the captured sequence of low-distortion images is used to reconstruct a 2D unwrapped image with size 3,600×1,500. It needs 180×75 subimages to completely register one internal thread with 15.3 mm in diameter and 20 mm in length. Figure 3 shows the reconstructed 2D unwrapped image of an internal thread obtained by the described approach. In this figure, the crest and root of the

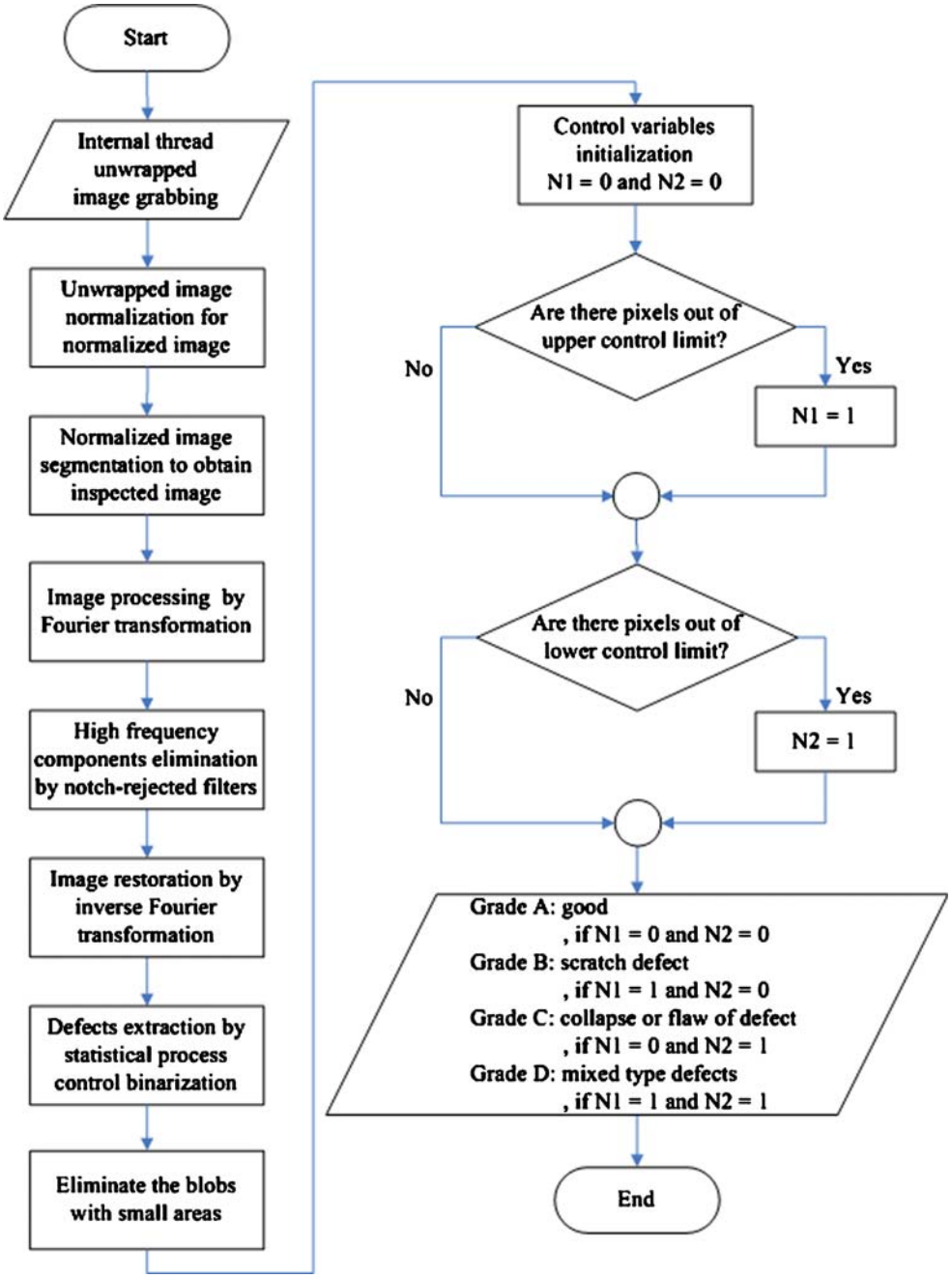

Fig. 2 Flowchart of the proposed OTPG algorithm

internal thread correspond to the wide and narrow white bands, respectively. The flanks of the internal thread appear as gray bands. A complete thread pattern is composed of a wide white band, a gray band, a narrow white band, and another gray band in that order. The inner surface of an internal thread is indeed a type of directional texture that comprises repetitive and periodic thread patterns.

3.3 OTPG algorithm

The most common defects in internal threads are collapses on the crest, scratches on the flank, and flaws in the root, as shown in Fig. 3. A scratch usually appears as a bulge that will cause an internal thread to bind with an external one, while a collapse or flaw appears as a cavity that will decrease the tight fit of a thread. This section focuses on developing an auto-inspection software, OTPG algorithm, to detect those defects that are embedded in homogeneous thread patterns. An implicit qualitative inspection algorithm [39] is used to detect the embedded defects. The OTPG algorithm includes four major operations: unwrapped image normalization, normalized image segmentation, thread pattern blurring, and defect extraction. These are discussed below.

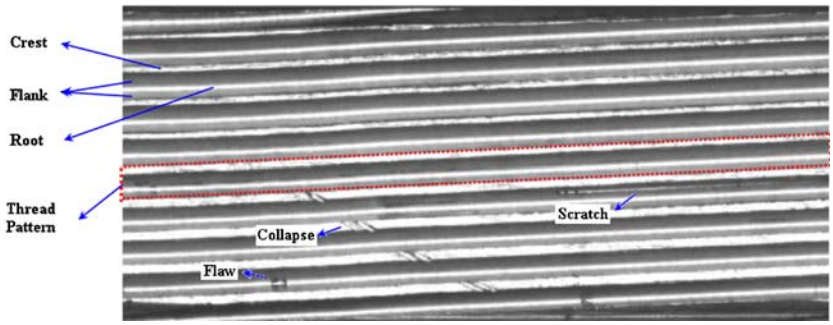

Fig. 3 Reconstructed 2D unwrapped image of an internal thread

3.3.1 *Unwrapped image normalization*

Because the internal thread is at some arbitrary orientation in relation to the OTPG fixture during defect inspection, the start point of the tapping process in the reconstructed unwrapped image will appear at some random location. To ensure that the relative position of the global structure of each unwrapped image coincide, we developed a process that can automatically reorient the start point of the tapping process in the unwrapped image so it is always on the right-hand side of the image. The procedure of normalizing the unwrapped image is described below and illustrated in Fig. 4.

The key to normalizing an unwrapped image is to find the start point of the tapping process of the internal thread and place it on the right-hand side of the image. To do this requires a good binary image where the foreground is composed of white bands (crests and roots) and the background is composed of gray bands (flanks). In addition, we need to locate the initial root in the binary image. The initial root is generated early in the thread tapping process. Therefore, if we track the intensity of each pixel of the binary image one-by-one, scanning from left to right and top to bottom, the frontier foreground element and the corresponding eight-connected elements must be the initial root.

Figure 3 shows an initial reconstructed unwrapped image of an internal thread. We first apply the grayscale closing operator with k1×k1 mask size (k1 is larger than one and is an odd integer) to fix the interspaces and fill up the holes; the result is shown in Fig. 4a. We then convert the grayscale image of Fig. 4a to a binary image using a threshold value calculated with Eq. 1 to separate the crests and roots from the flanks,

$$\text{threshold value} = \max(\mathbf{G}) - \text{k2} \tag{1}$$

where **G** is the universal set of gray values of Fig. 4a and k2∈[1, max(**G**)−1] is an offset constant. This produces the binary image of Fig. 4b. In Fig. 4b, we regard each eight-

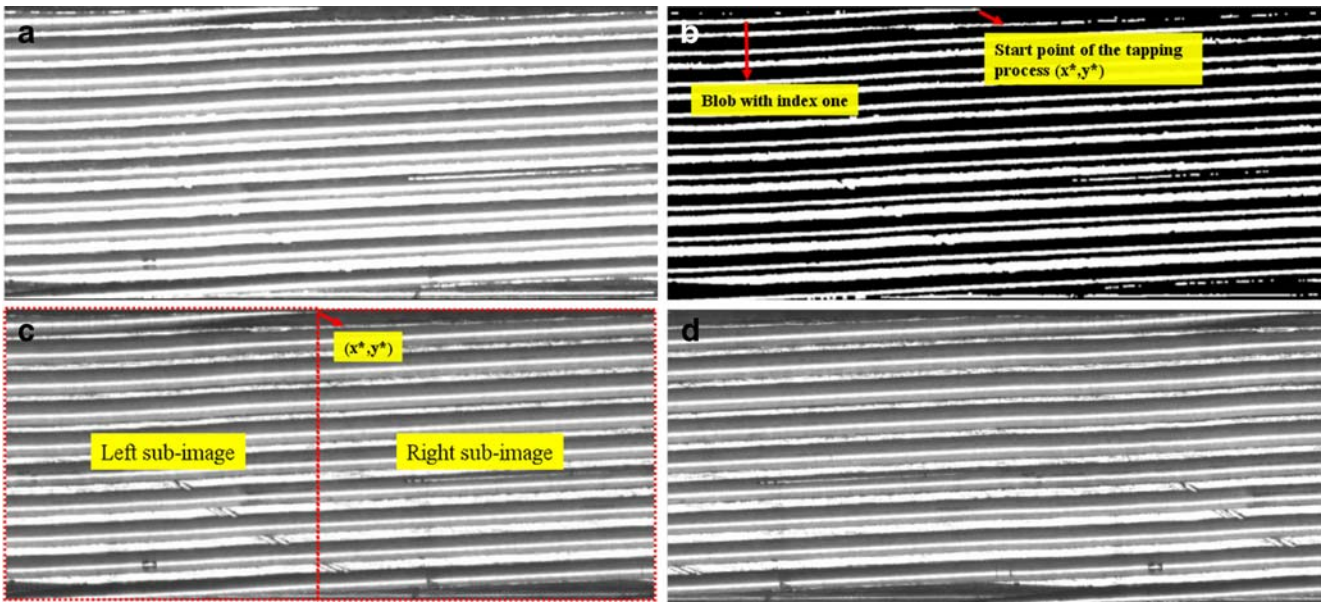

Fig. 4 Unwrapped image normalization procedure: **a** morphological image, **b** labeled image where the blob with index one is regarded as the initial root of the thread and its corresponding right-bottom coordinate (x^*, y^*) is the start point of the tapping process, **c** division of the unwrapped image into left and right subimages based on the (x^*, y^*) coordinate, and **d** normalized image generated from rounding the coordinate of the start point in **c** to the right-hand side

connected foreground element as a blob and apply a row-by-row labeling algorithm from left to right and top to bottom. The row-by-row labeling algorithm is guaranteed to find the initial root of an internal thread because it is the first one to be produced in the tapping process. The blob of the initial root is labeled as the index one and its corresponding right-bottom coordinate (x^*, y^*), the start point of the tapping process, is recorded. Then, we map (x^*, y^*) onto the unwrapped image of Fig. 3 and divide this image into left and right subimages, as shown in Fig. 4c, based on the x^* coordinate. The unwrapped image can be rounded arbitrarily due to the intrinsic cylindrical structure of the internal thread. We can obtain a normalized image by rounding the coordinate of the start point to the right-hand side, as shown in Fig. 4d. Note that this normalization operation can assure the repeatability of the unwrapped image; this is discussed further in Section 4.1.

3.3.2 Normalized image segmentation

Note that the first two and the last thread patterns of an internal thread can be ignored because the beginning and ending stages of the tapping process form relatively unstable and abnormal patterns. Moreover, these thread patterns are not important in the interaction with an external thread for creating a firm fastening. We focus only on the remaining thread patterns, named the inspected image, in the normalized image and so develop an automatic segmentation process. The normalized image segmentation procedure is explained below and illustrated in Fig. 5.

The inner surface of an internal thread comprises repetitive and periodic thread patterns. A scan along the line that extends from the top to the bottom in the vertical direction of (x^*, y^*) in Fig. 4b will touch on the initial root first, followed by the initial crest, followed by the second root, then the second crest, etc. This is the ideal case, however, because some noise blobs may interrupt the regularity. Thus, an efficient suboperation for eliminating the noise blobs is necessary.

Based on the results of Fig. 4b, we obtain a binary image where each blob has a unique labeling index. However, there are still some noise blobs in Fig. 4b especially distributed at the start and end of the crest. To eliminate them, we examine two properties of each blob: the area and the angle. The noise blobs with a small area or irregular angle relative to the angle of the crests and roots are eliminated. After applying this blob elimination suboperation on Fig. 4b, we obtain the clear labeled image shown in Fig. 5a. Then by scanning along a line that stretches from the top to bottom of the image in the vertical direction of (x^*, y^*), we can record the top coordinates of the third- and second-last roots. Based on the coordinates of the third- and second-last roots, we can determine upper and lower segmented bounds along the horizontal direction. Finally, the normalized image is trimmed based on these two segmented bounds, as shown in Fig. 5b, and the corresponding inspected image of size $m \times n$ is autosegmented, as shown in Fig. 5c.

3.3.3 Thread pattern blurring

We can observe a set of directional textures in the image to be inspected. The Fourier-based image restoration technique is well-suited for detecting defects in directional textures [32]. Intuitively, the dominating direction of the thread pattern in the inspected image will correspond to orthogonal straight lines throughout the center of the spectrum. The lines associated with high-energy frequency components in the spectral domain are eliminated by reducing them to zero and transforming back to the spatial

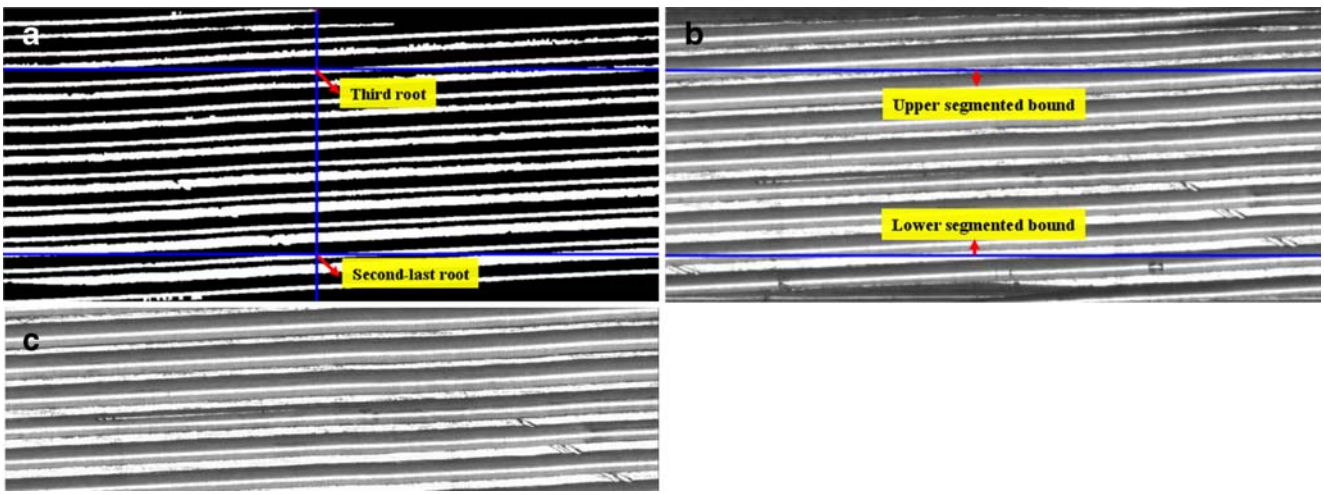

Fig. 5 Normalized image segmentation procedure: **a** start with a clear labeled image where the noise blobs have been eliminated and find the third and second-last roots, **b** map two segmented bound onto the normalized image of Fig. 4d, and **c** obtain final image to be inspected

domain. The procedure will blur all thread patterns and preserve only local defects if they are initially embedded in the inspected image.

Inspected image processing by Fourier transformation As shown in Fig. 5c, the thread patterns of the inspected image appear as a type of periodic directional texture. We first characterize the periodically occurring thread patterns according to their frequency components. Let $f(x, y)$ be the gray level of the pixel at x, y in the inspected image of size $m \times n$. The discrete 2D Fourier transformation is,

$$F(u,v) = \frac{1}{mn}\sum_{x=0}^{m-1}\sum_{y=0}^{n-1} f(x,y)\exp[-j2\pi(ux/m + vy/n)] \tag{2}$$

for frequency variables $u = 0, 1, 2, \ldots, m-1$ and $v = 0, 1, 2, \ldots, n-1$. Notice that we have multiplied $f(x, y)$ by $(-1)^{x+y}$ and shifted the origin of $F(u, v)$ to the frequency coordinates $(m/2, n/2)$. As shown in Fig. 6a, the global thread patterns are easily distinguishable as a concentration of high-energy lines in the spectrum that are orthogonal to the direction of thread pattern in Fig. 5c.

Eliminating high-energy frequency components elimination by notch-rejected filters Since thread patterns and scratch defects are oriented in the same direction in the inspected image, the thread patterns are mixed together with the orthogonal lines in the spectrum. Since orthogonal lines may be due to both thread patterns and scratches, using a band-rejected filter to eliminate the orthogonal, as reported by Tsai and Hsieh [32], is not an appropriate approach. In this paper, we map the wide dynamic range of $F(u, v)$ in Fig. 6a into a narrow range of $P(u, v)$ by a logarithm transformation and scale its intensity into an 8-bit gray level using,

$$P(u,v) = S[\log(1 + |F(u,v)|)] \tag{3}$$

where $S(.)$ is a scaling suboperation. Some high-energy frequency components in the spectrum image can then be determined in terms of a high-energy threshold and are set to zero by the notch-rejected filters described in,

$$F(u,v) = \begin{cases} 0 & \text{if } P(u,v) \geq k3 \\ F(u,v) & \text{otherwise} \end{cases}. \tag{4}$$

where k3∈[1, 255]. The resulting image is shown in Fig. 6b.

Image restoration using inverse Fourier transformation After eliminating the specific high-energy frequency components with notch-rejected filters, we back transform the spectrum image into the spatial domain using the inverse Fourier transformation (IFT),

$$\hat{f}(x,y) = \frac{1}{mn}\sum_{u=0}^{m-1}\sum_{v=0}^{n-1} F(u,v)\exp[\, j2\pi(ux/m + vy/n)] \tag{5}$$

for frequency variables $x = 0, 1, 2, \ldots, m-1$ and $y = 0, 1, 2, \ldots, n-1$. Then, a restored image is obtained from the real part of the IFT result by multiplying $(-1)^{x+y}$. In Fig. 6c, we observe that the homogenous thread patterns in Fig. 5c have been blurred and the associated gray levels have been compressed into a uniform and limited range. Conversely, the gray levels of scratches on the flank in Fig. 5c have been retained. Meanwhile, the gray levels of collapses on the crest or flaws in the root in Fig. 5c have been reduced.

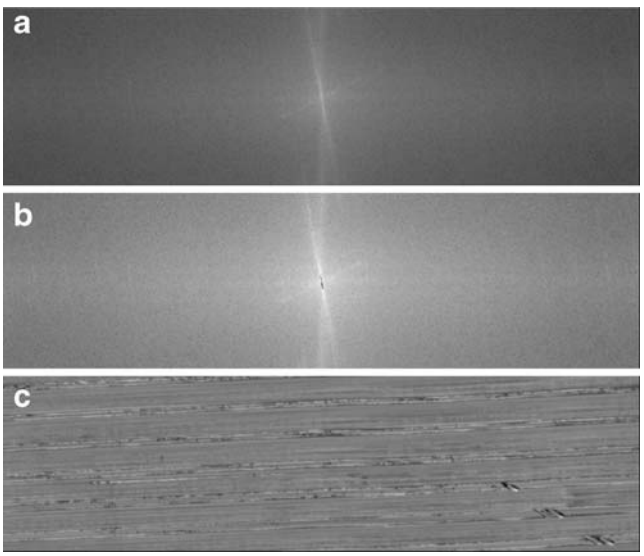

Fig. 6 Blurring the thread pattern of Fig. 5c: **a** spectrum image, **b** high-frequency elimination using notch-rejected filters, and **c** restored image

3.3.4 Defect extraction

Since the scratches are relatively brighter and the collapses or flaws are relatively darker than the blurred thread patterns in the restored image, as shown in Fig. 6c, we can use the statistical process control (SPC) binarization method [32, 35] to set the upper and lower control limits for determining defects from the uniform thread patterns. The SPC binarization method can be described by,

$$\hat{f}(x,y) = \begin{cases} 255 & \text{if } \mu_{\hat{f}} - \text{k4}\cdot\sigma_{\hat{f}} < \hat{f}(x,y) < \mu_{\hat{f}} + \text{k4}\cdot\sigma_{\hat{f}} \\ 0 & o.w. \end{cases} \tag{6}$$

where k4 is a control constant; $\mu_{\hat{f}}$ and $\sigma_{\hat{f}}$ are the mean and standard deviation, respectively, of the gray level in the restored image. If a pixel has a gray level that falls between the

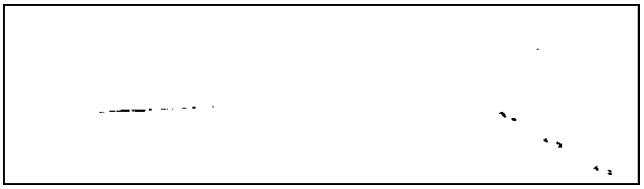

Fig. 7 Defect extraction procedure: the result of using the SPC binarization method on Fig. 6c where the small-area blobs have been removed

upper and the lower limits, it is shown as white and is considered to be a thread element that should be removed. Otherwise, it is shown as black and is considered to be a defective element that should be preserved. The result of applying the SPC binarization method on Fig. 6c is shown in Fig. 7 where the eight-connected component labeling procedure had applied to remove small-area noise blobs. The threshold for small-area noise blobs can be set in terms of the specification of requirement. In our study, the area threshold of 30 is adopted; it means that the minimal flaw that the OTPG can detect is approximate to $1.782\times10^{-4}\text{mm}^2\times30$.

4 Experiments and discussion

In Section 4.1, we describe the repeatability property of the normalized image already discussed in Section 3.3.1. A sample internal thread was placed at three arbitrary orientations to test the repeatability of the normalization. In Section 4.2, we describe some preliminary experiments to evaluate the impact of different values of these parameters. In Section 4.3, five samples of good and defective internal threads are used to demonstrate the inspection results of the proposed OTPG. Forty-four samples are used to evaluate effectiveness and robustness of the proposed OTPG. Furthermore, an oily sample is used to show that the proposed OTPG is against to pollution.

4.1 Repeatability property of the normalized image

To demonstrate the repeatability property of the normalized image, we permit the user to place the internal thread on the fixture at some arbitrary orientation. The original sequence of images is reconstructed by rounding the start point of the tapping process of the unwrapped image to the right-hand side.

As shown in Fig. 8a–c, three unwrapped images were reconstructed in arbitrary orientations. The three images differed only in their relative position. Applying the proposed image normalization procedure normalized all these images in the same manner, as shown in Fig. 8d. This shows that our normalization procedure can successfully normalize the unwrapped image so that the start point of the tapping process is always on the right-hand side. Such image position normalization also provides a uniform inspected image for defect detection.

4.2 Sensitivity analysis of parameter settings

As implemented, the OTPG algorithm described in Section 3.3 has four major parameters that influence the inspection outcome: the mask size of grayscale closing operator k1, the offset constant k2, the high-energy threshold k3, and the control constant k4.

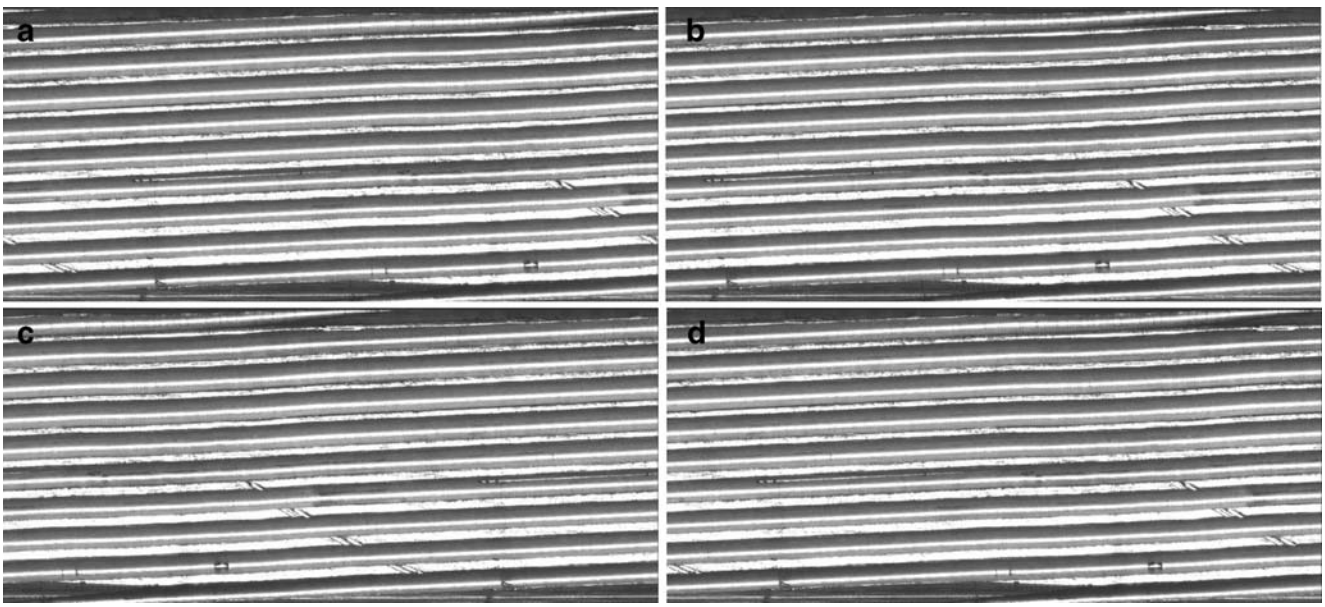

Fig. 8 Demonstration of repeatability: **a** first unwrapped image, **b** second unwrapped image, **c** third unwrapped image, and **d** corresponding normalized image

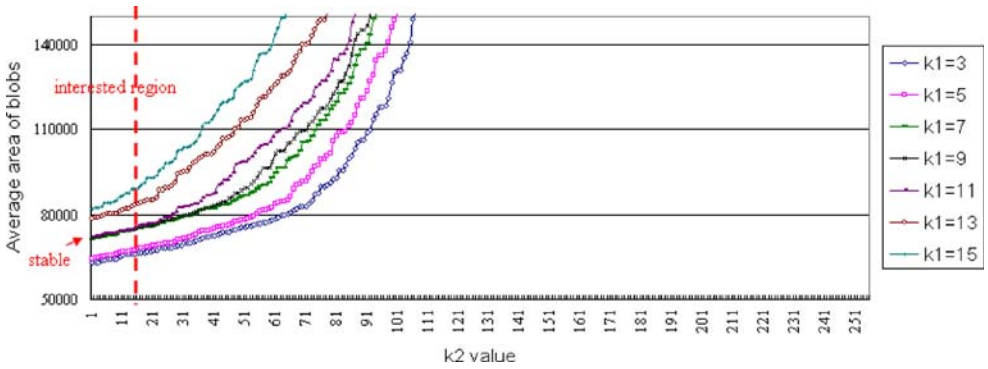

Fig. 9 Average area of blobs generated for different values of k1 and k2

4.2.1 Effects of the mask size of grayscale closing operator k1 and the offset constant k2

The parameter k1 is the rectangular size of the mask of grayscale closing operator that can mend the interrupted crests or roots in the internal thread image. The parameter k2 is an offset constant that can adjust the binary threshold value in Eq. 1 to enable the user to reveal the pixels with gray levels between max(**G**)−k2 and max(**G**) in Fig. 4a. The bright bands (crests or roots) and gray bands (flanks) in the morphological image of the internal thread can be well mended and totally separated if both k1 and k2 are selected properly. That permits the analysis of the normalization and segmentation procedures in Sections 3.3.1 and 3.3.2 to proceed successfully. In general, as the value of k1 or k2 increases, there are more and more crests and roots will join into the connected blobs. On the contrary, as the value of k1 or k2 decreases, neither the crest nor the root will be well shaped or well mended. Those blobs will appear as false crests or roots so that the image of the internal thread will be ambiguous and complicated for later processing.

To obtain reliable values of k1 and k2, a supervised pretraining session was conducted on 22 samples. Figures 9 and 10 showed the curves of the average area of blobs, and the average number of blobs after the blob elimination suboperation described in Section 3.3.2 was applied for different combinations of k1 and k2. The curves of different k1 in Fig. 9 were dramatically inflating when the values of k2 were larger than 25. Meanwhile, in Fig. 10, these curves were decreasing when the values of k2 were larger than 14 due to the bright and gray bands have gradually joined together. The intersection of the intervals, $k2 \geqq 25 \cap k2 \geqq 14$, was took the complement which yielded an interested region, $k2 < 14$, to be discussed as follows: When k1 was smaller than 5, the average areas of blobs were relatively low and the average numbers of blobs were relatively high due to interrupted crests or roots were not well mended and then were partial eliminated. When k1 was in the range of 7–11, the average area of blobs and the average number of blobs were relatively stable due to the crests and roots can be well mended and separated from the flanks reliably. When k1 was larger than 13, the average area of blobs were relatively high and the average number of blobs were relatively low due to some crests or roots have joined together by the large mask sizes that some blobs will be misinterpreted as false crests, roots, or flanks. In this way, we can get the stable intervals of k1 in the range of 7–11 and k2 less than 14.

4.2.2 Effect of the high-energy threshold k3

The high-energy threshold of Eq. 4 assists in producing notch-rejected filters to eliminate the high-energy frequency components in the spectrum. In general, a large value of k3 was used so that only one notch-rejected filter was generated at the center of the spectrum. The overall structure was retained in the corresponding restored image. An appropriate value of k3 was used to remove the periodic directional texture of the thread pattern while preserving the

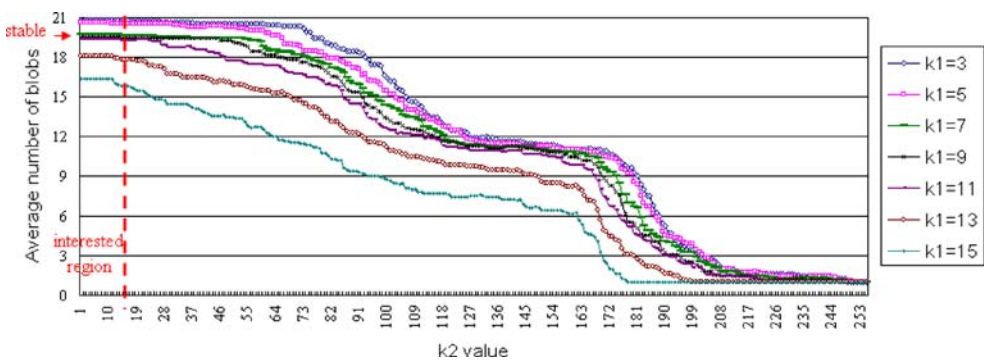

Fig. 10 Average number of blobs generated for different values of k1 and k2

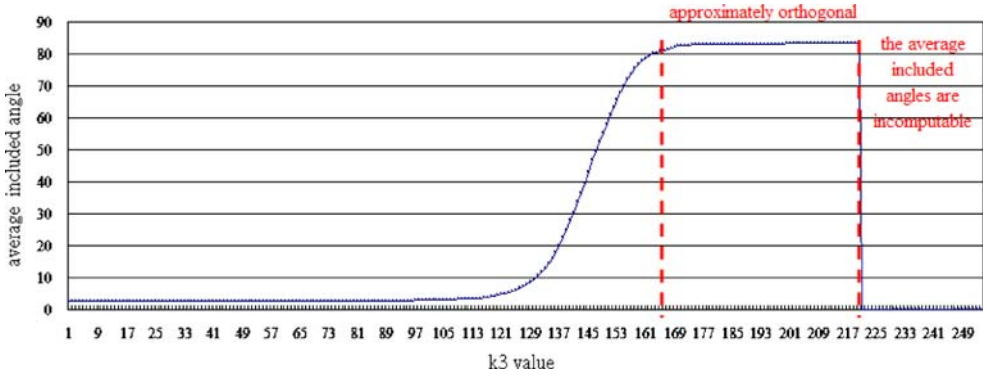

Fig. 11 Average included angles for different values of k3

defects. Note that the notch-rejected filters were allocated in a direction orthogonal to the thread pattern spread range near the center of the spectrum image only. A smaller value of k3 was selected to generate too many unnecessary notch-rejected filters so that the global structure and defects were all removed, leaving nothing meaningful.

Twenty-two samples were used to calculate the corresponding average angle of the notch filters in the Fourier domain. The included angles between the angle of thread pattern in the spatial domain and the angle of the notch filters in the Fourier domain are shown as functions of k3 in Fig. 11. The average included angles increased gradually when k3 was in the range of 1–168. When k3 was in the range of 168–220, the average included angles were approximately orthogonal. When k3 was greater than 220, only one notch filter was produced in the Fourier domain so that the corresponding average included angle could not be computed. Experience from the training samples indicates that a value between 168 and 220, where the average included angles are approximately orthogonal, is the most suitable. Using the middle value of 168 and 220, there is always an appropriate number of notch-rejected filters generated at appropriate positions in the spectrum.

4.2.3 Effect of the control constant k4

Since scratches are brighter and collapses and flaws are darker than blurred thread patterns in the restored image, the SPC binarization concept shown in Eq. 6 is used to distinguish between thread patterns and defects. The value of k4 affects the severity of the lower and upper control limits. In general, smaller values of k4 results in tight limits that the thread patterns might not been fully whitened and more noise appears in the binary image, i.e., false alarms. Conversely, a value of k4 that is too large results in a very relaxed standard that may white both the thread patterns and defects and produce missed detections.

Figure 12 shows the detection outcome based on 22 samples. The false alarm phenomenon decreased gradually as k4 increased and was the inverse of the missed detection phenomenon. Figure 12 also illustrates that SPC binarization yielded satisfactory limits with the highest number of correct detections and lowest number of false alarms and missed detections when k4 was in the range of 5.7–5.9.

4.3 Experimental results

In this section, we present some experimental results of internal thread inspection to confirm the function of the proposed OTPG. Figure 13a1–a5 shows inspected images of good or defective internal threads. The parameters generated from 22 training samples were k1=9, k2=7, k3=194, and k4=5.8 (to take the middle values of these corresponding recommended intervals). Figure 13b1–b5 shows the corresponding inspection results. A nondefective internal thread image resulted in a clear response; otherwise, defects were clearly indicated in their actual locations. As previously mentioned, a scratch will cause an internal

Fig. 12 Defect detection results for different values of k4

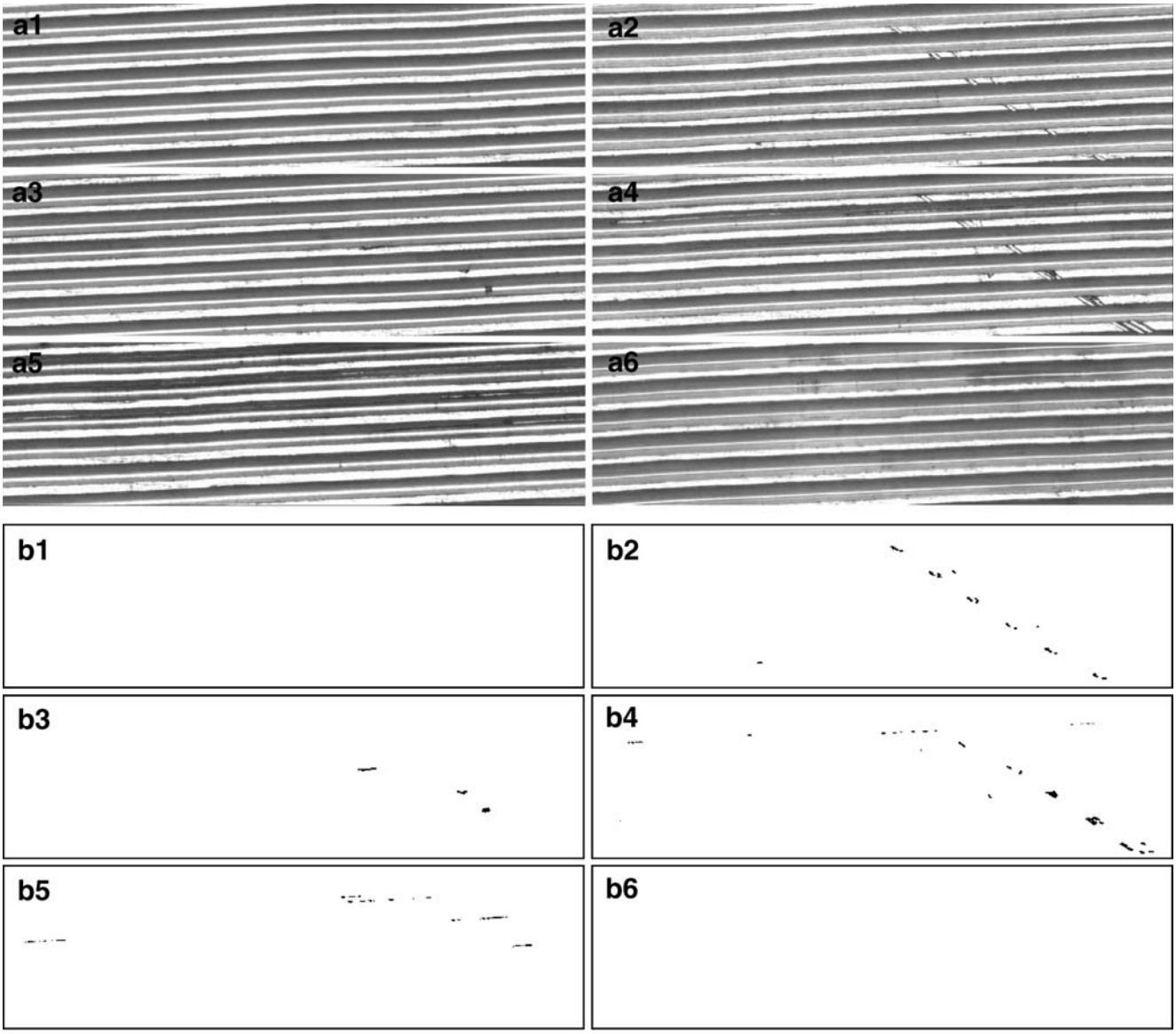

Fig. 13 Experimental test results of the proposed OTPG: **a1** good internal thread, **a2** defective internal thread with a collapse, **a3** defective internal thread with a collapse and flaw, **a4** defective internal thread with a collapse and scratch, **a5** defective internal thread with a scratch, **a6** polluted internal thread, and **b1**–**b6** the resulting binary images corresponding to **a1**–**a6**

thread to bind with an external one, and a collapse or flaw will decrease the tight fit. The pixels of a scratch were relatively bright and the pixels of a collapse or flaw were relatively dark compared to the blurred thread patterns in the restored image.

Forty-four testing samples (23 nondefective and 21 defective) were tested for evaluating the inspection rate of proposed method. After applying the proposed OTPG algorithm, we had no any false alarm but only one miss-detection; this meant that the inspection rate was up to 97.72%. The only miss-detection was due to the scratches on the flanks that were small and noncontinuous, so they were miss-regarded as small-area noise blobs to be miss-removed.

For quality assurance purposes, we classified the internal threads into four categories. First, when no blob existed in the final response image, this was classified as a good grade A internal thread. Second, when a blob existed in the final response image and the corresponding gray levels in the restored image were above the upper limit, this was classified as a scratched defective grade B internal thread that should be reworked by thread tapping to sweep away the bulges on the flanks. The third classification was the same as the second, except the gray levels that were below the lower limit; this was classified as a collapsed or flawed defective grade C internal thread that should be tested for close fit by a human expert. Fourth, when an internal

thread with a mixture of defects existed, this was classified as grade D for which both rework and fit testing are required.

Furthermore, as shown in Fig. 13a6, a nondefective sample polluted by the oil was tested based on the trained parameters. The oily thread surface was well blurred in the restored image and then be removed in the binarized image as shown in Fig. 13b6. The nondefective internal thread was correctly claimed with good quality regardless of it is polluted or not. That is to say, the OTPG can work against the polluted thread surface.

5 Conclusions and further researches

5.1 Conclusions

We proposed a novel OTPG for the auto-inspection of internal threads that provides an orientation-free internal thread placement mechanism. The system captures a sequence of partial wall 2D images of the internal thread that are converted to a 2D unwrapped image. We designed a preprocessing algorithm to achieve repeatability when segmenting the inspected image. We implemented a Fourier-based restoration technique to highlight defects such as scratches, collapses, and flaws in the directional texture image. A bulge-shaped scratch can be detected easily, but cave-shaped collapse or flaw is difficult to detect mechanically. The proposed OTPG duplicates and surpasses the capability of a mechanical gauge to test the functionality and tight fit on an internal thread.

5.2 Further researches

The reconstructed 2D image loses the depth information of an internal thread pattern. Some crucial features, such as the diameter and lead angle of the internal thread, are beyond the scope of this paper. The 3D reconstruction of internal threads to improve automated optical inspection measurement remains a subject for further research.

For the developed prototype OTPG, the inspection time includes image grabbing and image processing. The former inspection time takes 62.5 min and the latter one takes less than 6 s in inspecting an internal thread with diameter 15.3 mm and length 20 mm. The image registration time is the bottleneck of the OTPG approach. It is worth studying how to reduce the image registration time for further research.

Acknowledgments This research is partially supported by the National Science Council, Taiwan, under contract no. NSC 97-2221-E-009-112-MY3. We would particularly like to thank the reviewers who gave so much of their time in providing excellent feedback to the authors.

References

1. Hassel M (1994) A laser-based thread detection system. Sens Rev 14(3):18–19
2. Hassel M (1995) Laser-based feature detection system including internal thread detection. IEEE/IAS Int Conf Ind Autom Control Emerg Technol 567–568. doi:10.1109/IACET.1995.527621
3. Gore M (1996) Internal thread inspection with capacitive sensors. Sens 12:48–49
4. Tu DW, Tao J, Qi S (1998) Computer-aided internal thread parameters testing. Proc SPIE 3558:234–238. doi:10.1117/12.318391
5. Zhao Y, Li PS, Pu ZB (1999) MJ internal thread used for aerospace and its non-contact test method with a fiber optic sensor. Proc SPIE 3740:501–504. doi:10.1117/12.347727
6. Zhao Y, Liao YB (2002) Single-mode fiber-based reflex sensor for internal surface in-line measurement of small products. Sens Actuators A Phys 101(1–2):30–36. doi:10.1016/S0924-4247(02)00143-7
7. Zhao Y, Liao YB (2003) Research on measurement technology of internal MJ threads used for aerospace with a reflex fiber-optic sensor. Opt Eng 42(2):416–420. doi:10.1117/1.1532742
8. Field RH (2000) Detecting threads in machined holes: a look at eddy-current and other promising new probes. Manuf Eng 124 (6):96, 98, 100–101
9. Wang XM, He J, He FY (2002) Leakage magnet detection system for inside screw steel pipes and flaw identification. Heavy Mach 6:18–21 (In Simplified Chinese)
10. He FY, He J, Chen HD (2003) Inspection of the screw inside steel pipes and the testing system. Nondestruct Test 25(7):343–345, 368 (In Simplified Chinese)
11. Lin JM, Lee TB, Lei H, Zheng Y (2005) The rotate and scan technique of eddy current test on screw and internal thread inspection. Nondestruct Insp 29(5):28–31 (In Simplified Chinese)
12. Liu QM, Wang LS, Chen XW, Cui Z (2005) Non-damage measurement on internal taper thread of electrode. Opt Tech 31 (2):309–314 (In Simplified Chinese)
13. Lang WJ, George S (1988) Crampton and the origins of industrial endoscopy. Mater Eval 46:1639–1642
14. Parenti R, Verrecchia P, Bosla G, Pignone E (1994) Industrialized real-time flame thermal mapping system with off-line correction of spatial error. IEEE Int Conf Ind Electron Control Instrum 3:1977–1980. doi:10.1109/IECON.1994.398122
15. Tsushima T, Ishii A, Ochi Y, Masaoka N, Matsusue N (1997) Corrosion inspection of steel tube inner wall. IEEE/ASME Int Conf Adv Intell Mechatron 34. doi:10.1109/AIM.1997.652892
16. Boudjahi S, Ferreira A, Krupa A (2003) Modeling and vision-based control of a micro catheter head for teleopcrated in-pipe inspection. IEEE Int Conf Rob Autom 3:4282–4287. doi:10.1109/ROBOT.2003.1242262
17. Gu HT (2003) Industrial videoprobe's application in Chinese civil aviation maintenance. Test Equip Technol 6:56–57 (In Simplified Chinese)
18. Biegelbauer G, Vincze M, Nohmayer H, Eberst C (2004) Sensor based robotics for fully automated inspection of cores at low volume high variant parts. IEEE Int Conf Rob Autom 5:4852–4857. doi:10.1109/ROBOT.2004.1302486
19. Bondarev OY (2004) Application of industrial endoscope for the testing of a technical condition of a petroleum and gas industry objects. Kontrol' Diagn 3:23–25
20. Ahn J, Schobeiri MT, Han JC, Moon HK (2006) Film cooling effectiveness on the leading edge region of a rotating turbine blade with two rows of film cooling holes using pressure sensitive paint. J Heat Transf 128(9):879–888. doi:10.1115/1.2241945
21. Ahn J, Schobeiri MT, Han JC, Moon HK (2007) Effect of rotation on leading edge region film cooling of a gas turbine blade with

three rows of film cooling holes. Int J Heat Mass Transf 50(1–2):15–25. doi:10.1016/j.ijheatmasstransfer.2006.06.028
22. Perng DB, Liu CP, Chen YC, Chou CC (2002) Advanced SMD PCB vision inspection machine development. 15th IPPR Conf Comput Vis Graph Image Process, pp 311–317
23. Perng DB, Chou CC, Chen WY (2007) A novel vision system for CRT panel auto-inspection. J Chin Inst Ind Eng 24(5):341–350
24. Perng DB, Chen YC, Lee MK (2005) A novel AOI system for OLED panel inspection. J Phys Conf Ser 7th Int Symp Meas Technol Intell Instru 13(1):353–356
25. Chen LC, Kuo CC (2008) Automatic TFT-LCD mura defect inspection using discrete cosine transform-based background filtering and 'just noticeable difference' quantification strategies. Meas Sci Technol 19(1):015507. doi:10.1088/0957-0233/19/1/015507
26. Chen YC (2008) Automatic optical inspection system design for microrouter collapse inspection system. Dissertation, National Chiao Tung University
27. Perng DB, Chou CC, Lee SM (2007) Design and development of a new machine vision wire bonding inspection system. Int J Adv Manuf Technol 34(3–4):323–334. doi:10.1007/s00170-006-0611-6
28. Lewis JP (1995) Fast normalized cross-correlation. Vis Interface 120–123
29. Fitch AJ, Kadyrov A, Christmas WJ, Kittler J (2005) Fast robust correlation. IEEE Trans Image Process 14(8):1063–1073. doi:10.1109/TIP.2005.849767
30. Kumar A (2008) Computer-vision-based fabric defect detection: a survey. IEEE Trans Ind Electron 55(1):348–363. doi:10.1109/TIE.1930.896476
31. Xie X (2008) A review of recent advances in surface defect detection using texture analysis techniques. Electron Lett Comput Vis Image Anal 7(3):1–22
32. Tsai DM, Hsieh CY (1999) Automated surface inspection for directional textures. Image Vis Comput 18(1):49–62. doi:10.1016/S0262-8856(99)00009-8
33. Chan CH, Pang GKH (2000) Fabric defect detection by Fourier analysis. IEEE Trans Ind Appl 36(5):1267–1276. doi:10.1109/28.871274
34. Lambert G, Bock F (1997) Wavelet methods for texture defect detection. Int Conf Image Process 3:201–204. doi:10.1109/ICIP.1997.632054
35. Tsai DM, Chiang CH (2003) Automatic band selection for wavelet reconstruction in the application of defect detection. Image Vis Comput 21(5):413–431. doi:10.1016/S0262-8856(03)00003-9
36. Ngan HYT, Pang GKH, Yung SP, Ng MK (2005) Wavelet based methods on patterned fabric defect detection. Pattern Recognit 38(4):559–576. doi:10.1016/j.patcog.2004.07.009
37. Tsai DM, Wu SK (2000) Automated surface inspection using Gabor filters. Int J Adv Manuf Technol 16(7):474–482. doi:10.1007/s001700070055
38. Mak KL, Peng P (2008) An automated inspection system for textile fabrics based on Gabor filters. Robot Comput Integr Manuf 24(3):359–369. doi:10.1016/j.rcim.2007.02.019
39. Newman TS, Jain AK (1995) Survey of automated visual inspection. Comput Vis Image Underst 61(2):231–262. doi:10.1006/cviu.1995.1017